EARTH SURFACE PROCESSES AND LANDFORMS
Earth Surf. Process. Landforms **45**, 2432–2449 (2020)

Published online 14 June 2020 in Wiley Online Library
(wileyonlinelibrary.com) DOI: 10.1002/esp.4889

High spatio-temporal resolution measurements of cohesive sediment erosion

Felix Beckers,[1]* Caleb Inskeep,[1] Stefan Haun,[1] Gerhard Schmid,[1] Silke Wieprecht[1] and Markus Noack[1,2]
[1] Institute for Modelling Hydraulic and Environmental Systems, Department of Hydraulic Engineering and Water Resources Management, University of Stuttgart, Pfaffenwaldring 61, Stuttgart 70569, Germany
[2] Faculty of Architecture and Civil Engineering, Karlsruhe University of Applied Science, Moltkestrasse 30, Karlsruhe 76133, Germany

Received 23 December 2018; Revised 29 April 2020; Accepted 1 May 2020

*Correspondence to: Felix Beckers, Institute for Modelling Hydraulic and Environmental Systems, Department of Hydraulic Engineering and Water Resources Management, University of Stuttgart, Pfaffenwaldring 61, 70569 Stuttgart, Germany. E-mail: felix.beckers@iws.uni-stuttgart.de

ESPL
Earth Surface Processes and Landforms

ABSTRACT: In this study, we present a novel approach to measure fundamental processes of cohesive sediment erosion. The experimental setup consists of a laboratory erosion flume (SETEG) and a photogrammetric method to detect sediment erosion (PHOTOSED). Detailed data are presented for three erosion experiments, which were conducted with a natural non-cohesive/cohesive sediment mixture at increasing sediment depths (4, 8, 16 cm). In each experiment, the sediment was exposed to a set of incrementally increasing shear stresses and the erosion was measured dynamically, pixel-based, and approximate to the process scale given the resolution of PHOTOSED. This enables us to distinguish between (i) individual emerging erosion spots caused by surface erosion and (ii) large holes torn open by detached aggregate chunks. Moreover, interrelated processes were observed, such as (iii) propagation of the erosion in the longitudinal and lateral direction leading to merging of disconnected erosion areas and (iv) progressive vertical erosion of already affected areas. By complementing the (bulk) erosion volume profiles with additional quantitative variables, which contain spatial information (erosion area, specific deepening, number of disconnected erosion areas), conclusions on the erosion behaviour (and the dominant processes) can be drawn without requiring qualitative information (such as visual observations). In addition, we provide figures indicating the spatio-temporal erosion variability and the (bulk) erosion rates for selected time periods. We evaluate the variability by statistical quantities and show that significant erosion is mainly confined to only a few events during temporal progression, but then considerably exceeds the time-averaged median of the erosion (factors between 7.0 and 16.0). Further, we point to uncertainties in using (bulk) erosion rates to assess cohesive sediment erosion and particularly the underlying processes. As a whole, the results emphasise the need to measure cohesive sediment erosion with high spatio-temporal resolution to obtain reliable and robust information. © 2020 The Authors. Earth Surface Processes and Landforms published by John Wiley & Sons Ltd

KEYWORDS: PHOTOSED; SETEG; cohesive sediments; non-cohesive/cohesive sediment mixtures; photogrammetric measurements; spatio-temporal erosion variability

Introduction

Detailed knowledge regarding the erodibility and erosion behaviour of cohesive sediments and non-cohesive/cohesive sediment mixtures is of particular importance for many engineering and ecological applications. Consequently, many studies investigate the influence of sediment characteristics and the eroding fluid on the erodibility of cohesive sediments and non-cohesive/cohesive sediment mixtures, or intend to approximate these relationships mathematically (e.g. Gularte *et al.*, 1980; Mehta and Partheniades, 1982; Raudkivi and Tan, 1984; Berlamont *et al.*, 1993; Mitchener and Torfs, 1995; Panagiotopoulos *et al.*, 1997; Black *et al.*, 2002; Tolhurst *et al.*, 2006; Gerbersdorf *et al.*, 2007; Righetti and Lucarelli, 2007; Mostafa *et al.*, 2008; Noack *et al.*, 2015; Perera and Wu, 2016; Wu *et al.*, 2018). Although sizeable progress has been made in uncovering relations between sediment properties and erodibility (Grabowski *et al.*, 2011), cohesive sediment erosion has not yet been fully understood.

In order to improve this understanding, more reliable laboratory and field data are needed (e.g. Zhu *et al.*, 2008; Grabowski *et al.*, 2011; Wu, 2016). This demand can be met with ongoing experimental research using various existing erosion devices. An overview on available *in-situ* devices and measurement techniques can be found in Black and Paterson (1997) and Aberle (2008), who make a classification from recirculating flumes, flow-through flumes, and other miscellaneous devices. Examples of miscellaneous devices include jet-testing apparatuses (Hanson and Cook, 2004) and cohesive strength meters (Paterson, 1989). The erosion flumes can be further subdivided into straight open flumes, closed tunnels, and annular flumes,

[Correction added on 30 June 2020 after first online publication: the formatting of Table 3 has been amended, and the overbar and tilde symbols have been corrected in Table 4 and the caption of Figure 2 in this version.]

which have been used for field experiments but are also used for laboratory investigations as well (e.g. Wu *et al.*, 2018). While an advantage of *in-situ* devices is that they can be operated over undisturbed beds (Black and Paterson, 1997) where non-disturbing placement is possible, their disadvantage is that they can only be used to erode surface sediment layers (Noack *et al.*, 2015). However, many engineering and ecological issues require depth-dependent information on the erodibility of sediments, such as the assessment of the vertical erosion risk of buried contaminated sediments (e.g. McNeil *et al.*, 1996; Gerbersdorf *et al.*, 2007) or the assessment of the vertical erosion potential of reservoir deposits (e.g. Beckers *et al.*, 2018). To serve this purpose, laboratory flumes have been developed and applied to measure the depth-dependent erosion behaviour (e.g. McNeil *et al.*, 1996; Kern *et al.*, 1999; Briaud *et al.*, 2001; Lick and McNeil, 2001; Roberts *et al.*, 2003; Righetti and Lucarelli, 2007; Jacobs *et al.*, 2011; Kimiaghalam *et al.*, 2016). Their design follows a general principle: sediment core samples are locked into an erosion channel from below. The sediment is then slowly raised into the current and the time to erode the protruding sediment is measured to provide a bulk erosion rate (i.e. the bed elevation changes over time). The sediment response to changing flow conditions is tested, eventually results in a set of erosion rates as a function of flow, and standard methods are used to calculate the corresponding shear stress (Walder, 2016).

Many of the existing erosion devices, both *in-situ* and laboratory devices, use optical backscatter sensors to measure suspended-sediment concentration during erosion experiments, which is then used to calculate the resuspension rate (e.g. Mehta and Partheniades, 1982; Amos *et al.*, 1992; Black *et al.*, 2002; Aberle, 2008; Droppo *et al.*, 2015). The disadvantage of the latter is that the resuspension rate cannot necessarily be equated with the erosion rate, due to the fact that the bed load may contribute to cohesive sediment erosion, especially when dealing with non-cohesive/cohesive sediment mixtures (Mitchener and Torfs, 1995; Roberts *et al.*, 2003; Aberle *et al.*, 2004; Debnath *et al.*, 2007; Wu, 2016). Thus, recent studies have aimed to address this point by complementary measurements, including bed load traps or bed elevation monitoring (e.g. Roberts *et al.*, 2003; Debnath *et al.*, 2007; Jacobs *et al.*, 2011; Ye *et al.*, 2011). However, even if resuspension rates are complemented with additional bed load measurements, they result in a bulk erosion rate with respect to the available measuring area, although cohesive sediment erosion is described as a highly dynamic process due to the temporal and spatial variability of naturally composed sediments (Black *et al.*, 2002; Gerbersdorf *et al.*, 2007; Aberle, 2008). Further, the non-uniformity of natural sediments results in variable bed shear strength and, in combination with the turbulent characteristic of flow, a random behaviour is induced during erosion (e.g. Van Prooijen and Winterwerp, 2010; Schäfer Rodrigues Silva *et al.*, 2018).

Following non-cohesive erosion modes, two principle modes of cohesive sediment failure are typically described in the literature: surface erosion and mass erosion. While the first is characterised by particle or floc erosion of surficial sediments triggered by the fact that the shear strength is locally exceeded by the flow forces, the latter is the response of the bed to a dynamic shear load (Mehta and Partheniades, 1982), resulting in the erosion of clusters or lumps of aggregates (Zhu *et al.*, 2008) or even in the erosion of layers due to bed failure along planes (Wu *et al.*, 2018). Mehta and Partheniades (1982) identified two main erosion types, referred to as *Type I* and *Type II*, through an interpretation of time–concentration profiles of bulk resuspension rates. They differ in that under constant shear stress over time, *Type I* erosion asymptotically decreases and approaches a constant value, whereas *Type II* erosion does not. The cause of this behaviour is the vertical stratification of a sediment bed, and either uniform or non-uniform bed shear strength over depth. This is why these erosion types are also classified as depth-limited or supply-limited erosion (*Type I*) and steady-state or unlimited erosion (*Type II*) (e.g. Parchure and Mehta, 1985; Aberle, 2008; Van Prooijen and Winterwerp, 2010). However, the transition between these erosion types might be smooth and does not allow for a clear distinction (Grabowski *et al.*, 2011). Consequently, complementary descriptions can be found that combine features of both types (e.g. Amos *et al.*, 1992; Debnath *et al.*, 2007; Aberle, 2008). Yet, all these erosion types describe a bulk erosion effect and do not make a distinction between the underlying erosion processes, although specific erosion forms have been visually observed in studies on cohesive sediments.

McNeil *et al.* (1996) report that, during erosion, individual particles are entrained before chunks of sediment are plucked from the surface, leaving holes or pits behind. Righetti and Lucarelli (2007) observe a multistep entrainment phenomenon and distinguish between a sporadic, discontinuous motion of relatively small aggregates, followed by an increasing number of primary particle aggregates, coupled with the sporadic entrainment of larger aggregates. Finally, a gradual enhancement of floc entrainment is observed, until an abrupt change in the erosive process takes place, which is described as a sudden increase in quantity and size of the eroded flocs. Kothyari and Jain (2008) describe the entrainment of clumps and layers, and identify three stages of initiation of motion: pothole, line, and mass erosion.

Although a considerable variety of experimental studies can be found in the literature, very little information is available on measurement technology that is capable of resolving the spatial and temporal variability of the cohesive erosion process (see Tolhurst *et al.*, 2006; Van Prooijen and Winterwerp, 2010). However, high-resolution measurement data are a pending requirement when it is intended to objectively assess the highly variable erosion progress of cohesive sediments. In this context, dynamically measured erosion caused by specific erosion forms could help to increase knowledge on the fundamental as well as interacting processes.

In this study, we propose a novel approach based on high-resolution photogrammetric measurements for detailed investigations of cohesive sediment erosion, including quantitative evaluations of the spatio-temporal erosion variability. First, we introduce our apparatus, consisting of an erosion flume (SETEG) and a photogrammetric method to detect sediment erosion (PHOTOSED). This includes the hydraulic characterisation of the flume and the derivation of the measurement variables provided by PHOTOSED. Next, we show for three experiments a selection of the spatio-temporal erosion progress, illustrate the ability of our approach to identify fundamental erosion processes caused by specific erosion forms, and present the full temporal development of erosion profiles containing spatial information. We narrow these results down to characteristic changes in the erosion behaviour, assess the spatio-temporal erosion variability by statistical quantities, and present the erosion rates derived from the volumetric measurements. Finally, we critically discuss our results and the key findings of this study. We expect that obtaining high spatio-temporal resolution data will help in identifying the fundamental erosion processes and eventually increase our knowledge on the erosion of cohesive sediments and non-cohesive/cohesive sediment mixtures.

Materials and Methods

SETEG erosion flume

The SETEG erosion flume (*erosion flume to determine the depth-dependent erosion stability of aquatic sediments*) is

located at the Institute for Modelling Hydraulic and Environmental Systems (IWS, University of Stuttgart). It is a straight, rectangular, and closed flume to measure critical shear stresses and erosion rates of sediments over depth. The flume is operated under pressurized flow (Kern *et al.*, 1999) and has been continuously developed further to address challenges in sediment research (Witt and Westrich, 2003; Noack *et al.*, 2015, 2018). The setup of the SETEG-erosion flume is presented in Figure 1. The dimensions are as follows: length 8.00 m, width 0.142 m, and height 0.10 m (inner dimensions). The flow is measured with a magnetic flow meter (MFM, Endress+Hauser, Promag 50W1F DN150, error ≤ 0.5%) and can be controlled by the operator to investigate flow rates from 1 up to 65 l s^{-1}. The measuring section consists of a circular opening in the flume bottom where sediment cores with diameters between 100 and 135 mm can be locked in position. The centre of the measuring section is located 7.64 m downstream of the inflow. By means of a piston and a lifting spindle, the sediment sample can be moved vertically to position various sediment layers at individually selected core depths. When a desired layer is reached, the vertical movement stops and the protruding sediment is cut off with a wire (using a specially designed apparatus). It is removed from the flume, leaving the sediment layer flush with the bottom. Through this minimally invasive procedure, each experiment begins with a user-set/defined hydraulic condition. Furthermore, the removed sediment can be used to study the sediment characteristics. Next, the erosion experiment starts and the sediment surface is exposed to incrementally increasing flow rates and, consequently, incrementally increasing shear stresses. They are applied for constant time periods to study the temporal erosion behaviour until surface failure is observed. This procedure is carried out for various sediment layers to obtain depth-dependent information on the erodibility of the investigated sediment (Beckers *et al.*, 2018). Given the pressurized flow conditions and the surrounding glass walls, all-round visibility is given as well as access for hydraulic (LDV) and photogrammetric (PHOTOSED) measurements.

Hydraulic characterisation and calibration

For the range of possible flow rates (Q = 1–65 l s^{-1}), the Reynolds number based on the hydraulic radius of the SETEG-erosion flume is constantly high (Re ≥ 8.3 × 10^3) and the entrance length for fully turbulent flow development can be approximated as 4.7 m (Nikuradse, 1932). In order to ensure a fully developed turbulent flow field and to obtain a hydraulic calibration function (Q–τ relation), we conducted high-resolution 2D laser Doppler velocimetry (LDV) measurements (TSI Inc., Shoreview, MN, USA). The setup of the LDV is shown in the upper panel of Figure 1. It was located on a traversal structure and mounted with the probe head axis at an angle of 8° in air (6° in water) to the bottom and perpendicular to the flume. During the measurements we used the software's coincidence mode (TSI Inc., 2011) to collect the velocity data in the longitudinal and vertical direction simultaneously. One single measurement at one position was completed once 20000 valid samples were collected. In total, 168 points per flow rate were measured to characterise the flow field. Each point is referred to a local coordinate system, where y (mm) denotes the direction of flow, z (mm) the vertical direction, and x (mm) the lateral direction. Points were distributed on four longitudinal cross-sections located 11 cm upstream (y400), 2 cm upstream (y310), in the centre (y290), and 2 cm downstream (y270) of the measuring section (with respect to the centre). On the vertical axis,

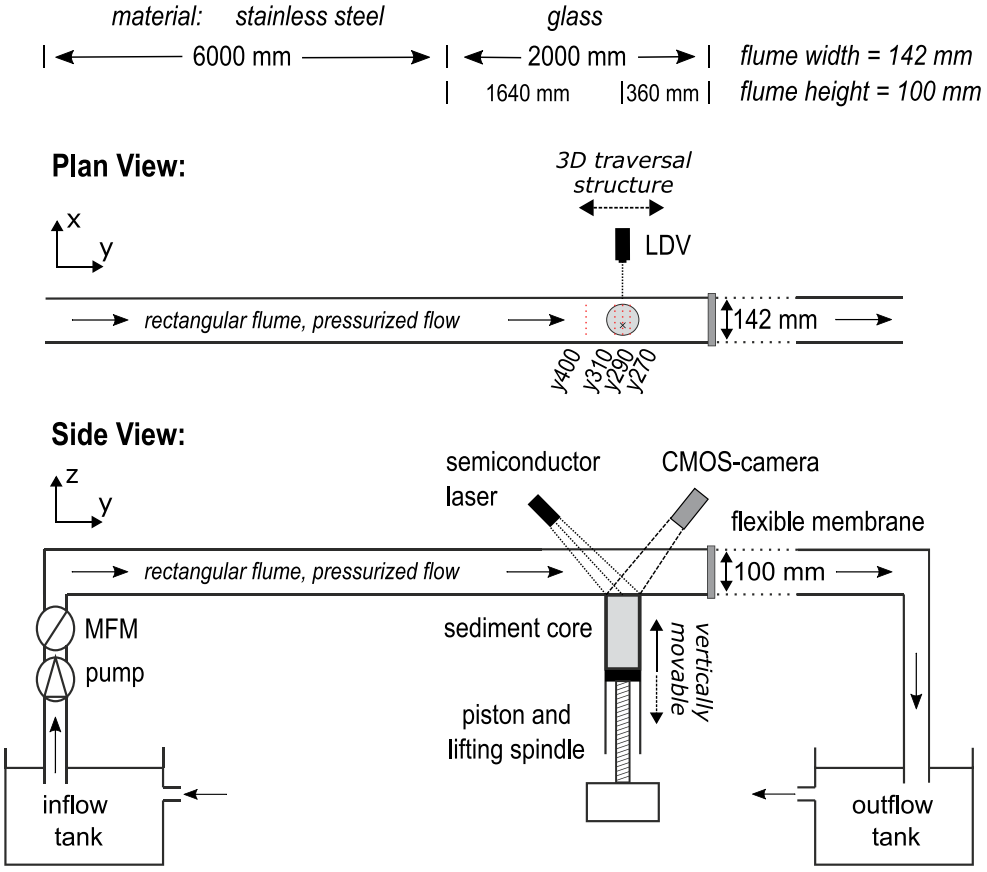

Figure 1. Schematic plan and side view of the SETEG erosion flume with dimensions. The measurement setup of a 2D LDV (plan view) and PHOTOSED (side view) are included (modified from Kern et al., 1999; Witt and Westrich, 2003; Noack et al., 2018). [Colour figure can be viewed at wileyonlinelibrary.com]

seven points were measured at increasing height positions. The lowest accessible position was 2 mm (z154) above the bed and, due to symmetry considerations, the highest measured point was the centre of the flume located 50 mm (z106) above the bed. The remaining positions were irregularly distributed at the following positions above the bed: 4 mm (z152), 6 mm (z150), 10 mm (z146), 18 mm (z138), and 34 mm (z122). Along a cross-section the velocity components were measured at six points (x220, x230, x240, x250, x260, x270).

From the measured velocity components, we calculate the mean velocity and the velocity fluctuations using Reynolds' decomposition, which is generally written as $u_i=\overline{u_i}+u'_i$. Here, u_i are the instantaneous (measured) velocity components, $\overline{u_i}$ are the time-averaged velocities, u'_i are the turbulent fluctuations, and i denotes the ith component of the velocity vector. Based on the spatially resolved measurements, we calculate the double-averaged velocity components commonly used in environmental hydraulics (e.g. Nikora *et al.*, 2007): $\langle u_i\rangle=\langle\overline{u_i}\rangle+\langle u'_i\rangle$. Here, the angle brackets denote the additional spatial averaging.

In our case, i=1,2; the double-averaged near-bed Reynolds shear stress can be derived for a specific flow rate $Q^*\rightarrow\tau^*$ from u'^* and v'^* according to

$$\tau^*=-\rho\left\langle\overline{u'^*v'^*}\right\rangle \tag{1}$$

where τ^* is the near-bed Reynolds shear stress, ρ is the fluid density, and $\left\langle\overline{u'^*v'^*}\right\rangle$ is the double-averaged (time and space) covariance of the longitudinal and vertical velocity fluctuations at a considered flow rate Q^*.

The hydraulic calibration curve is created by correlating the evaluated shear stresses with their corresponding flow rates. For this curve, the measured points at 2 mm (z154) above the flume bed are selected from the three cross-sections located along the measuring section (y310, y290, and y270). By means of this Q–τ relation, the near-bed Reynolds shear stress is derived at discrete values along the curve. The range of shear stresses applied in this study, and their evaluated spatial standard deviations, are provided in Table 1. The values of the standard deviations indicate that the spatial shear stress variation is approximately 11% on average.

Both the mean flow and the turbulence development is shown in Figure 2 by means of vertical distributions for two flow rates, namely 2 and 10 l s^{-1}. The measurements were conducted over a smooth surface as this represents the initial condition at the start of an erosion experiment. Figure 2a contains the double-averaged flow profiles and Figure 2b contains the covariance of the longitudinal u' and vertical v' velocity fluctuations. The Reynolds numbers are 1.7×10^4 (2 l s^{-1}) and 8.3×10^4 (10 l s^{-1}). Both flow and turbulence development is ensured, since the profiles show a good degree of fit along the vertical for all four longitudinal cross-sections.

PHOTOSED

The PHOTOSED method (photogrammetric sediment erosion detection) was developed for erosion measurements for a variety of cohesive and non-cohesive/cohesive sediment mixtures (Noack *et al.*, 2018). The PHOTOSED setup consists of a semiconductor laser with a diffraction optic (Laser2000 GmbH, Wessling, Germany) that is mounted diagonally over the measuring section of the SETEG erosion flume at an angle of 41° in air (59° in water) against the flow direction (see Figure 1). This allows us to project a structured light pattern consisting of approximately 24 000 light points (for a maximum core diameter of 135 mm) on the investigated sediment layer. During an erosion experiment, the sediment surface and displacement of light points is continuously monitored with a CMOS camera (2 MP, 10 Hz, Imaging Development Systems GmbH, Obersulm, Germany). The camera is mounted diagonally across the laser and captures images at an angle of 35° in air (41° in water) against the flow direction (see Figure 1). In a post-processing routine, consecutive frames are extracted from the captured time series at given time intervals. These files are then further processed using a Python script, which applies Farnebäck's Dense Optical Flow algorithm (Farnebäck, 2003) from the OpenCV library (Open Source Computer Vision, OpenCV 2.4.10) to calculate the erosion volumes within a user-specified, rectangular region of interest (ROI). PHOTOSED enables the detection of volumetric changes from approximately 1 mm^3 between two consecutive frames, provided the erosion takes place over an area of 35 pixels (corresponding to approximately 10 mm^2). A detailed technical description of PHOTOSED and the intense calibration and verification process can be found in Noack *et al.* (2018).

An image captured with the CMOS camera prior to the start of an erosion experiment, showing the projected light points, can be seen in Figure 3a. The ROI used in this study is also shown, denoted in yellow. The ROI was defined with a minimum distance of 1.5 cm from the core boundary to minimise possible boundary effects. It is worth noting that the scaling of the captured images is pixel-based. During post-processing, a conversion to metric scale is performed based on the known metric positions, resulting in a parallelogram as shown in Figure 3b.

Measurement outputs and variables

PHOTOSED detects the topographic change of a sediment surface during erosion for consecutive time frames within a neighbourhood block for each pixel. The system provides the elevation change $\Delta z^{(j)}$ per pixel, defined as

$$\Delta z^{(j)}=z^{(j)}_{t+\mathrm{d}t}-z^{(j)}_t \tag{2}$$

where $\Delta z^{(j)}$ (mm) is the elevation change per pixel j (j=1,...,n) defined by the ROI, t and t+dt define the time steps of two consecutive frames separated by the time interval dt, and $z^{(j)}$ is the instantaneous elevation per pixel.

Table 1. Relationship between flow rates (Q) and near-bed Reynolds shear stresses (τ) in the SETEG erosion flume including spatial standard deviation (SD). The shear stresses are derived from a Q–τ relation that was obtained from LDV measurements (2 mm above the bed, three cross-sections over measuring section). The values in bold denote the measured flow rates

Q (l s^{-1})	**1.0**	1.5	**2.0**	2.5	**3.0**	3.5	**4.0**	4.5	**5.0**	**6.0**	7.0	8.0	**10.0**
τ (Pa)	**0.04**	0.07	**0.10**	0.13	**0.17**	0.22	**0.27**	0.32	**0.38**	**0.50**	0.65	0.81	**1.18**
SD (Pa)	**0.005**	0.009	**0.012**	0.016	**0.020**	0.025	**0.029**	0.035	**0.040**	**0.052**	0.064	0.078	**0.109**

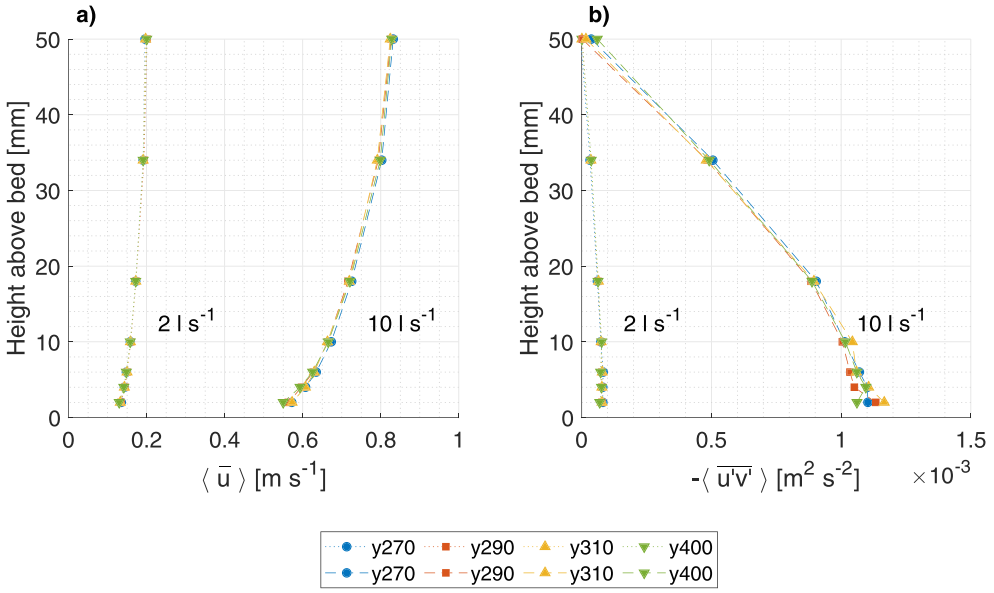

Figure 2. Flow and turbulence development in the form of double-averaged vertical distributions for four longitudinal cross-sections (located 11 cm upstream (y400), 2 cm upstream (y310), in the centre (y290), and 2 cm downstream (y270) of the measuring section). (a) Longitudinal velocity $\langle \overline{u} \rangle$ for 2 and 10 l s^{-1} and (b) covariance of the longitudinal and vertical velocity fluctuations $-\langle \overline{u'v'} \rangle$ for 2 and 10 l s^{-1}. [Colour figure can be viewed at wileyonlinelibrary.com]

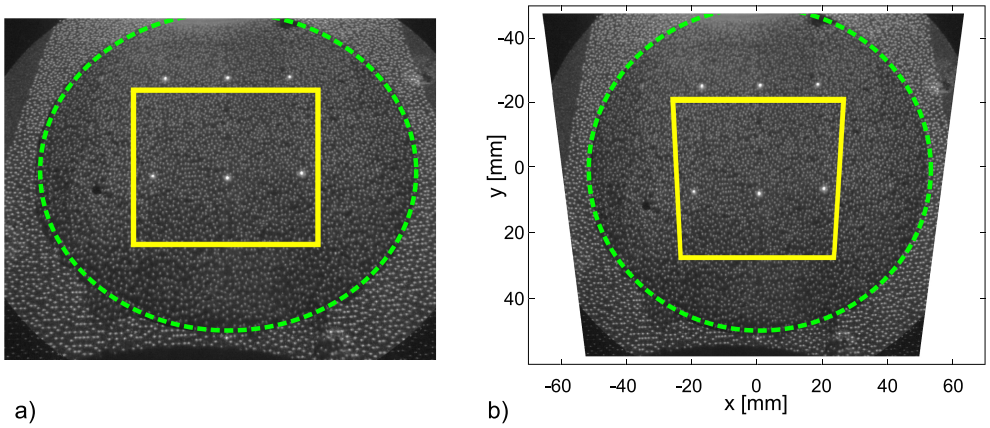

Figure 3. Image showing the initial state of the sediment surface before the start of the erosion experiment in (a) pixel scale and (b) metric scale. The green circle denotes the sediment core boundary, and the yellow square indicates the region of interest used in this study (A_{ROI} = 2642 mm^2). [Colour figure can be viewed at wileyonlinelibrary.com]

The erosion volumes for two consecutive time steps can be calculated as follows:

$$V_t^{(j)} = z_t^{(j)} \Delta x^{(j)} \Delta y^{(j)} \tag{3}$$

$$V_{t+dt}^{(j)} = z_{t+dt}^{(j)} \Delta x^{(j)} \Delta y^{(j)} \tag{4}$$

where $V_t^{(j)}$ and $V_{t+dt}^{(j)}$ (mm^3) are the erosion volumes, and $\Delta x^{(j)}$ and $\Delta y^{(j)}$ are the known metric length dimensions of pixel j in the domain defined by the ROI.

With Equations 3 and 4, we can calculate the erosion volume difference per pixel:

$$\Delta V^{(j)} = V_{t+dt}^{(j)} - V_t^{(j)} = \left(z_{t+dt}^{(j)} - z_t^{(j)} \right) \Delta x^{(j)} \Delta y^{(j)} = \Delta z^{(j)} \Delta x^{(j)} \Delta y^{(j)} \tag{5}$$

Aggregation of the discrete values obtained from Equation 5 over all pixels j, in the area defined by the chosen ROI, provides the spatially averaged erosion volume difference

$$\Delta V = \sum_{j=1}^{n} \Delta V^{(j)} \tag{6}$$

Next, a spatially averaged deepening is calculated by dividing the spatially averaged erosion volume by the area of the ROI (A_{ROI}):

$$\Delta z = \frac{\Delta V}{A_{ROI}} \tag{7}$$

where Δz (mm) is the average deepening, ΔV is the spatially averaged erosion volume difference between two consecutive time frames, and A_{ROI} is the area of the entire ROI. The erosion rate results from a division of Equation 7 by the considered time interval between the two consecutive frames:

$$\varepsilon = \frac{\Delta V}{A_{ROI}\,\mathrm{d}t} \tag{8}$$

where ε (mm s^{-1}) is the erosion rate, and dt (s) is the considered time interval.

As a result of the high spatial resolution of PHOTOSED, individual and disconnected areas of erosion can be detected. These individual erosion areas can be aggregated to a total area of erosion

$$A_e = \sum_{i=1}^{m} a_i \tag{9}$$

where A_e (mm^2) is the aggregated erosion area of all individual erosion areas, a_i (i=1,...,m) (mm^2) is the area of an individual erosion area, and m is the total number of individual erosion areas.

Subsequently, the specific deepening can be derived from Equation 7 by replacing the area of the ROI (A_{ROI}) with the aggregated area of erosion (A_e) obtained from Equation 9. Consequently, the specific deepening can be written as follows:

$$\Delta z_s = \frac{\Delta V}{A_e} \tag{10}$$

where Δz_s (mm) is the specific deepening.

Advantages and versatility

The ROI and time intervals are variable and can be specified during data evaluation due to the photogrammetric approach. This allows the user to select an ROI with sufficient distance from the core boundary to exclude possible boundary effects and to adapt the evaluation according to the observed erosion behaviour, for instance by modifying the considered time step while the ROI is kept constant. For example: the ROI is constant (A_{ROI} = 2642 mm^2) and the time interval is dt = 15 s. According to Equation 8 and the detection limits of PHOTOSED (Δz_{min}~ 0.1 mm on approximately 10 mm^2), the minimum detectable erosion rate is ε = 2.5 × 10^{-5} mm s^{-1}. Whereas if we integrate over a time interval of dt = 30 s, the minimum detectable erosion rate is ε = 1.3 × 10^{-5} mm s^{-1}. An added benefit of PHOTOSED is that the captured time series of frames may be reviewed at any time to verify the data and to ensure the reliability of the results. Furthermore, the measurements are insensitive to the transport mode after erosion due to the photogrammetric approach.

A specific example summarising the relevant advantages of the method is given in Figure 4. It shows enlarged segments of four consecutive frames (dt = 1 s) taken during an erosion experiment. The segments display the top right corner of a sediment surface, the ROI (yellow), and the sediment core boundary (green). An aggregate chunk gets detached within a second (between t = 111 and 112 s) at the top right corner of the ROI. It is apparent that this erosion is not triggered by any boundary effect, since the ROI was defined with sufficient distance from the core edge (1.5 cm, see also Figure 3).

Experimental procedure and sediment characterisation

This study presents the data of three erosion experiments (EI, EII, EIII). They have been conducted within a sediment core (diameter 10 cm) obtained from a reservoir located in the northern Black Forest, Germany (48°39′25″ N, 8°19′29″ E) on 26 September 2017. The experiments have been conducted at increasing vertical core depths. These depths were 4, 8, and 16 cm (measured from the top level of sediment). Each sediment surface was exposed to a set of shear stresses, applied consecutively and kept constant for t = 600 s. The increments of increase were chosen in such a way that the critical shear stress was exceeded during each erosion experiment. Table 2 summarises the investigated shear stresses for the three conducted erosion experiments.

Table 3 summarises depth-dependent sediment characteristics. The bulk density was measured using a gamma-ray densitometer (Beckers *et al.*, 2018), the total organic carbon (TOC) was determined by loss on ignition (DIN EN 13137, 2001), and particle size measurements were conducted with a Malvern Mastersizer 2000 (Malvern Instruments Ltd, Malvern, UK) that works with the principle of laser diffraction. The composition of the sediment mixture is given according to the classification scale of Wentworth (1922).

Results

Spatio-temporal evaluation of erosion progress

Figure 5 visualises the spatio-temporal erosion progress for erosion experiments EI, EII, and EIII at selected time steps. The selection was made since no relevant erosion was detected during the previously applied shear stresses (later confirmed by Figure 11) and due to the large collection of data. The figures are obtained by rolling out the pixel-based measurements ($\Delta z^{(j)}$) as cumulated values to the entire area of the ROI (A_{ROI} = 2642 mm^2). For this purpose, a time interval of dt = 100 s was chosen and the erosion progress is shown in the xy-plane for three time steps (t = 200, 400, and 600 s). For better presentation, the results are shown in pixel scale since the conversion to metric scale would result in a parallelogram according to Figure 4b. It should be emphasised that the edge of the subfigures corresponds to the edge of the ROI and not to the edge of the sediment core, as a minimum distance of 1.5 cm from the core

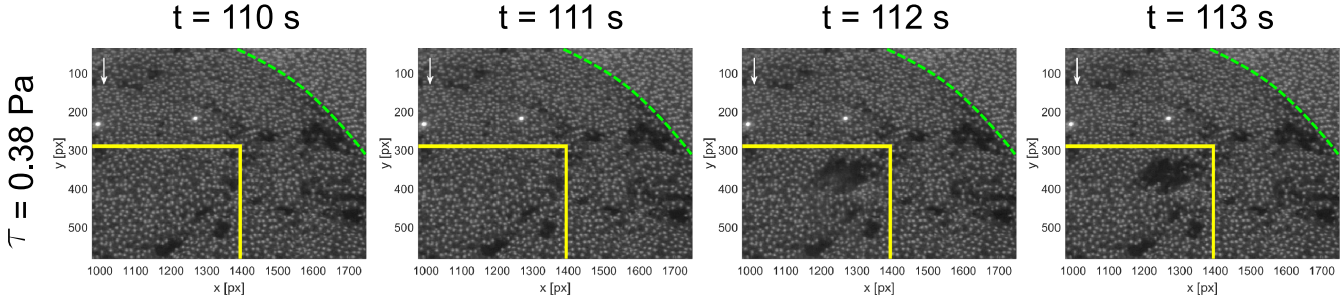

Figure 4. Four consecutive frames separated by a time interval of dt = 1 s, indicating the detachment of an aggregate chunk in the top right corner of the ROI (yellow) during an erosion experiment. The green line denotes the sediment core boundary. [Colour figure can be viewed at wileyonlinelibrary.com]

Table 2. Consecutively applied shear stresses for erosion experiment EI, EII, and EIII. Each shear stress was kept constant for $t = 600$ s. Detailed results are presented for selected shear stresses, which are denoted in bold

Name	Sediment layer (cm)	Shear stress (Pa)										
EI	4	0.07	0.10	0.13	**0.17**	**0.22**	0.27	0.32	0.38	0.50	0.65	
EII	8		0.10	0.13	0.17	0.22	0.27		**0.38**	**0.50**		
EIII	16				0.17		0.27		0.38	0.50	**0.65**	**0.81**

Table 3. Depth-dependent sediment characteristics over core depth

Sediment layer (cm)	Sediment composition (%)			Percentiles (μm)			Bulk density (g m^{-3})	TOC (%)
	Clay	Silt	Sand	d_{10}	d_{50}	d_{90}		
4	2.5	76.2	21.3	4.7	21.3	96.7	1.04	13.8
8	2.4	71.4	26.2	5.0	24.2	127.1	1.05	12.3
16	3.3	80.6	16.1	3.8	18.1	72.3	1.09	9.1

boundary is maintained (see Figures 3 and 4). The white arrow in the first subfigures denotes the flow direction (top to bottom).

The sediment surface in EI was least resistant towards erosion and experienced surface erosion (caused by flocs and small aggregates) during the first, second, and third applied shear stresses. This led to individual erosion spots with depths up to 1.7 mm by the end of $\tau = 0.13$ Pa (Figure 5b). Individual erosion spots of similar magnitude were further detected throughout the total duration of the erosion experiment, as a result of the same (surface) erosion processes.

During the higher shear stresses presented in Figures 5c and d, a variety of aggregates were detached from the surface. Consequently, these erosion forms created large spatial erosion areas through propagation in the flow and lateral direction, which resulted in the merging of individual erosion areas. Moreover, progressive vertical erosion was detected, as confirmed by Figures 5a–d. Yet parts of the surface remained unaffected by erosion at the end of $\tau = 0.22$ Pa (Figure 5d).

The sediment surface in EII initially showed a similar response compared to EI (4 cm). It experienced randomly distributed surface erosion, indicated by emerging individual erosion spots that did not exceed depths of more than 1.6 mm during shear stresses of $\tau = 0.22$, 0.27, and 0.38 Pa (Figures 5e–g). However, the applied shear stresses that initiated sporadic surface erosion differed by, on average, a factor of 2.8. The last applied shear stress ($\tau = 0.50$ Pa) tore large holes (maximum depth 8.1 mm) into the surface, which decreased in magnitude over time and formed a lateral connected erosion pattern by the end of the experiment (Figure 5h).

EIII was most resistant towards erosion, although a distinct erosion hole with a depth of 5.9 mm emerged upon increase to a shear stress of $\tau = 0.38$ Pa (Figure 5i). This event was caused by the detachment of a single aggregate chunk (the event is captured in Figure 4). In contrast, EII showed surface erosion for the same applied shear stress (Figure 5g). During the next two shear stresses ($\tau = 0.50$, 0.65 Pa), new individual erosion spots could be detected resulting from entrained flocs and aggregates (maximum depth 2.7 mm). Compared to similar erosion forms measured in EI, this results in a shear stress increase by an average factor of 5.0. During the last shear stress ($\tau = 0.81$ Pa), additional material was torn from the surface and a second distinct erosion hole opened up at the end with a depth of 4.6 mm (Figure 5l). It is worth noting that the initially emerged erosion hole did not deepen further during the proceeding erosion experiment.

Identification of erosion processes and relation to specific erosion forms

In each of the experiments, recurring erosion patterns have been detected. They were caused by different erosion processes and indicate that specific erosion forms are dominant during progressing erosion. In particular, two processes can be identified: (i) individual erosion spots emerging sporadically on the sediment surface and (ii) large holes that were torn open during erosion.

Figure 6 illustrates process (i) and Figure 7 illustrates process (ii). Both figures represent an extract from the previous Figure 5. They are thus equivalently evaluated for $dt = 100$ s. For clarification purposes, the upper panels show the relative erosion between the presented time steps, while the lower panels show the cumulative (absolute) erosion at each time step (see also Figure 5). While the first process is an effect of surface erosion and is indicative of floc and aggregate entrainment (Figure 6), the second process reveals local bed failure as a result of detached aggregate chunks (Figure 7).

During temporal progression of the erosion, interrelated processes could be measured and identified. These were (iii) a propagation of the erosion in the longitudinal as well as the lateral direction, leading eventually to merging of separated erosion areas and (iv) progressing vertical erosion (ongoing deepening). Examples of these interrelated processes are illustrated in Figures 8, 9, and 10. Again, the top panels indicate the relative erosion and the lower panels the cumulative (absolute) erosion at each time step. The processes shown are also taken from the time series provided in Figure 5. It is worth noting that these interrelated processes can be caused by new emerging individual erosion spots as a result of surface erosion (Figure 8) and by the formation of large holes through the detachment of aggregate chunks (Figure 9).

Given the relative erosion in the top panels and the cumulative erosion in the lower panels, the processes (i)–(iv) can be clearly identified in the presented examples in Figures 6–10. Moreover, from the measured processes one can infer the cause of specific erosion forms.

Temporal development of erosion profiles containing spatial information

For a combined comparison of the entire erosion results of the experiments (EI, EII, and EIII), Figure 11 contrasts the temporal development of (a) the erosion volumes (ΔV), (b) the erosion

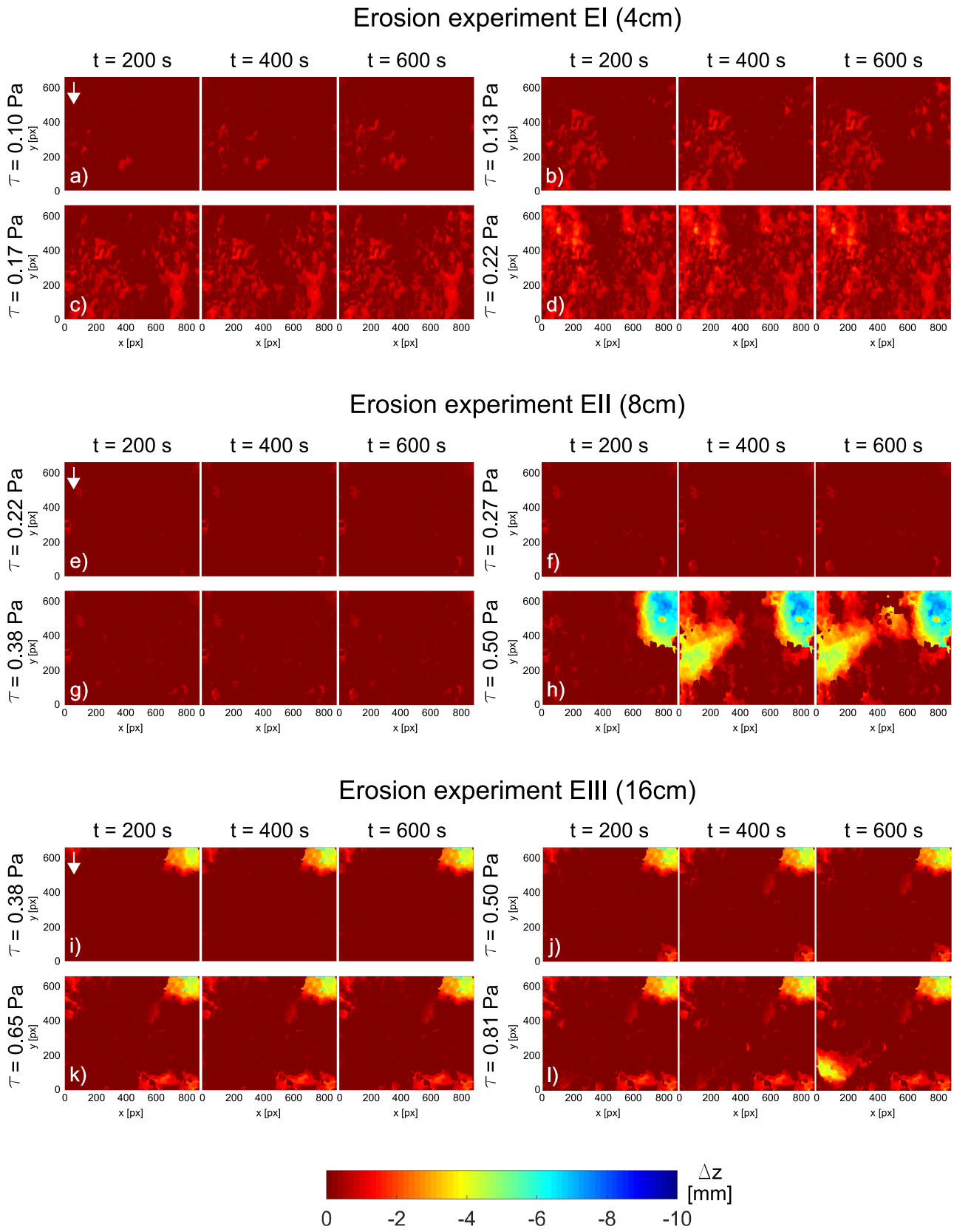

Figure 5. Spatial distribution of the cumulative erosion progress within the entire ROI (A_{ROI} = 2642 mm^2) for four consecutively applied shear stresses: experiment EI (4 cm), experiment EII (8 cm), and experiment EIII (16 cm). The erosion progress during each applied shear stress is shown at time steps t = 200, 400, and 600 s. The white arrow in the top left subfigure denotes the flow direction. [Colour figure can be viewed at wileyonlinelibrary.com]

areas (A_e), (c) the specific deepening (Δz_s), and (d) the number of disconnected erosion areas (m). All variables contain the aggregated results throughout the entire ROI. The erosion volume and area are displayed as cumulative values. Since the increments of the consecutively applied shear stresses differ among the experiments, some gaps exist for EII and EIII, as indicated in Table 3.

As expected, the profiles of the erosion volume initially show no response, because we deliberately started each erosion experiment below a critical erosion threshold. At the end of the

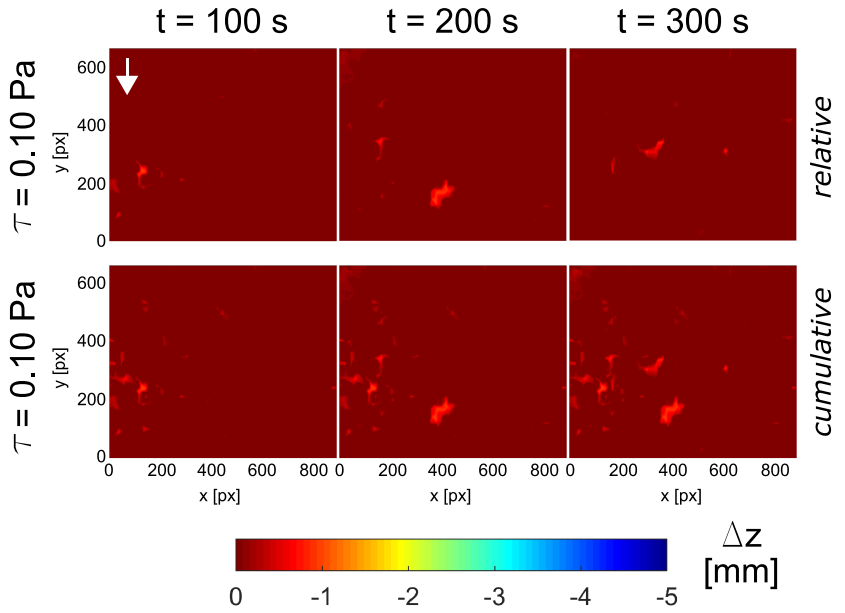

Figure 6. Example from experiment EI (4 cm) for sporadically emerging individual erosion spots. [Colour figure can be viewed at wileyonlinelibrary.com]

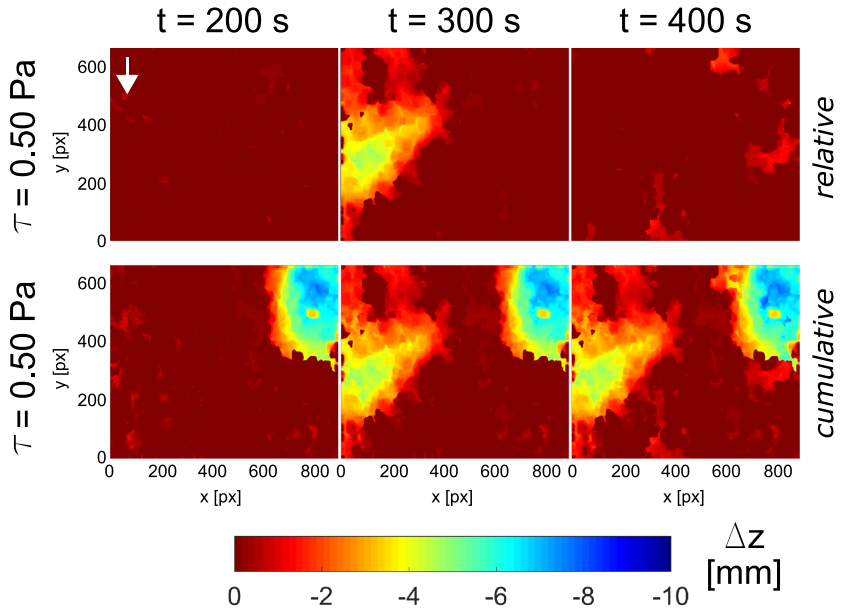

Figure 7. Example from experiment EII (8 cm) for the formation of large holes. [Colour figure can be viewed at wileyonlinelibrary.com]

experiments, the largest erosion volume is measured for EI (5504 mm^3), followed by EII (4113 mm^3) and finally EIII (1174 mm^3). In experiment EI, the final erosion affected an area of 2582 mm^2 (98%), while in EII it affected 1754 mm^2 (66%), and in EIII it affected 1068 mm^2 (40%). However, in EI most of the area was already affected in an early stage of the experiment (τ = 0.22 Pa), whereas in EII and EIII the surface experienced erosion at a later stage (τ = 0.50 and 0.38 Pa, respectively), as confirmed by Figure 5.

The significance of the actual occurring erosion is reflected in the specific deepening, since it relates the eroded volume to the affected area (Figure 11c). Consequently, distinct erosion events of high significance were measured in EII with a specific deepening of 2.9 mm (τ = 0.50 Pa) and in EIII with a specific deepening of 1.9 mm (τ = 0.38 Pa). These events could be attributed to deep holes torn into the surface by the sudden detachment of aggregate chunks, as confirmed by Figures 5e–l (see also Figure 7). In contrast, the profile of the specific deepening of EI does not contain events of comparable significance. This can be explained by the erosion mainly being characterised by a variety of individually emerging erosion spots to indicate continuous surface erosion (confirmed by Figures 5a–d; see also Figure 6). As a result, the sediment surface in EI was not prone to sudden failure like the deeper located surfaces (EII and EIII).

The disconnected erosion areas follow a general trend, which is shown to be consistent for each experiment (Figure 11d). First, the number of disconnected erosion areas increases continuously, indicating new emerging erosion areas. This can be traced back to sporadic surface erosion and suggests the entrainment of flocs and small aggregates, since the erosion volume and area affected stay relatively low. The initial rise of

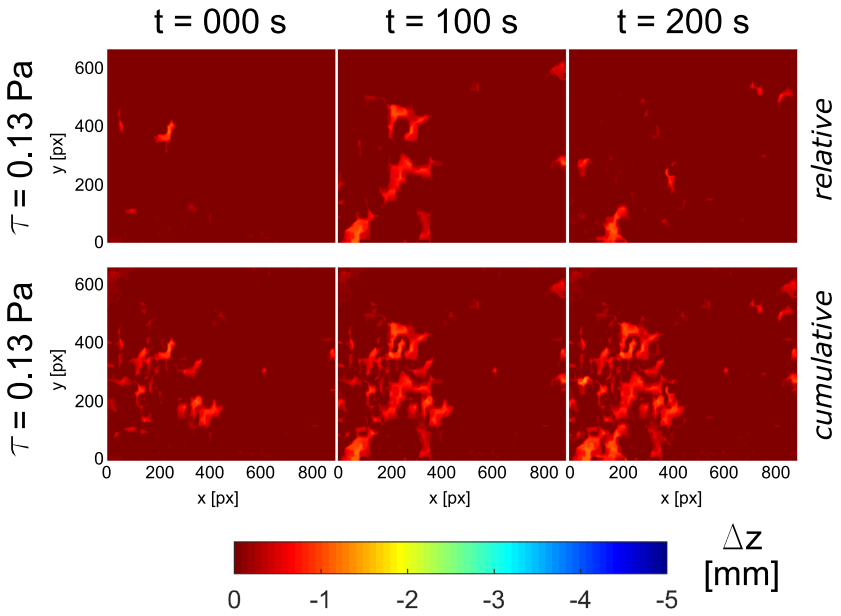

Figure 8. Example from experiment EI (4 cm) for the propagation of the erosion in longitudinal as well as lateral direction induced by individual emerging erosion spots. [Colour figure can be viewed at wileyonlinelibrary.com]

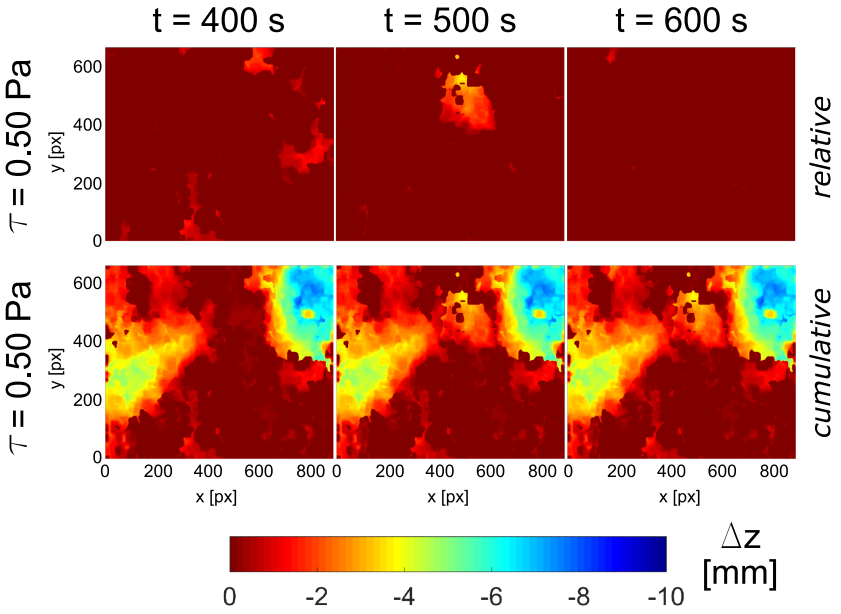

Figure 9. Example from experiment EII (8 cm) for the propagation of the erosion in longitudinal as well as lateral direction induced by the formation of erosion holes. [Colour figure can be viewed at wileyonlinelibrary.com]

the disconnected erosion areas was detected for EI at a shear stress of τ = 0.07 Pa, for EII at a shear stress of τ = 0.17 Pa, and for EIII at a shear stress of τ = 0.27 Pa. Second, a drop in the number of disconnected areas coincides with an increase in the erosion volume and erosion area, indicating that the erosion behaviour has changed – since disconnected erosion areas must have grown together while erosion proceeds (see also Figure 5). This characteristic case was measured for EI at a shear stress of τ = 0.17 and 0.22 Pa, and for EII at a shear stress of τ = 0.50 Pa. It is not as clear for EIII, but a similar trend was measured at the end of a shear stress of τ = 0.81 Pa (Figure 11). Based on these results, the following time periods were selected for detailed evaluation in the following section: EI (4 cm): τ = 0.17 and 0.22 Pa; EII (8 cm): τ = 0.38 and 0.50 Pa; EIII (16 cm): τ = 0.65 and 0.81 Pa (see also Table 3).

In general, it can be observed that the erosion decreased from EI to EIII, thus over the sediment core depth. This is indicated by the staggered arrangement of the erosion volume and the erosion area, as well as by the temporal offset in the disconnected erosion areas (Figure 11). As a result, the sediment characteristics in Table 2 indicate that erosion decreased with a higher bulk density, a refinement of the sediment composition, and a decreasing organic content.

Spatio-temporal erosion variability for selected time periods

Figures 12a–f show the range of detected erosion for the two consecutively applied shear stresses that were selected based

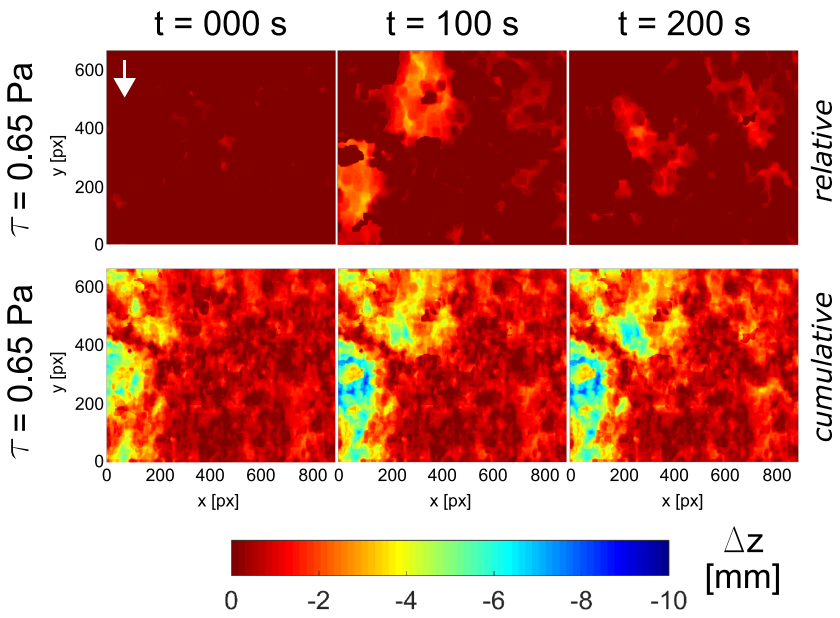

Figure 10. Example from experiment EI (4 cm) for progressing vertical erosion (ongoing deepening). [Colour figure can be viewed at wileyonlinelibrary.com]

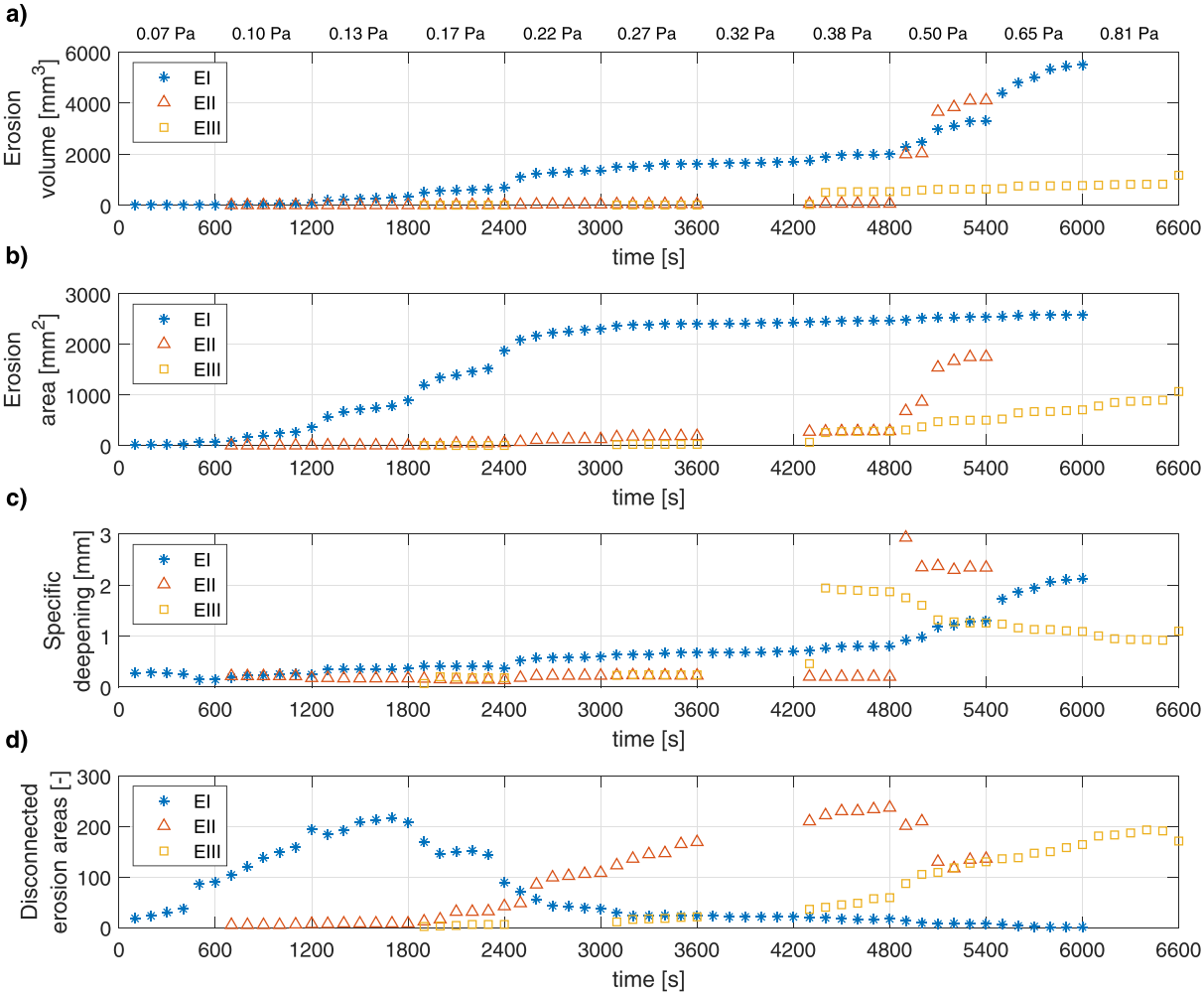

Figure 11. Comparison of (a) erosion volume, (b) erosion area, (c) specific deepening, and (d) number of disconnected erosion areas for the three conducted erosion experiments EI (4 cm), EII (8 cm), and EIII (16 cm). The evaluation was conducted with a time step of dt = 100 s. The consecutively applied shear stresses are listed above the upper panel. [Colour figure can be viewed at wileyonlinelibrary.com]

on the characteristic temporal change in the erosion behaviour (see also Table 3). The distribution of the erosion ($\Delta z^{(j)}$) is presented by means of boxplots and their concurrent bar graphs, which provide information about the aggregated erosion area (A_e). The time interval has been refined to dt = 30 s to obtain a higher temporal resolution. In doing so, the spatial erosion variability can be shown while still being able to group the data temporally. The central mark (denoted by the hollow circle) represents the median, the top and bottom of the blue box represent the 25th and 75th percentiles, respectively, and the whiskers cover the data that are not considered to be outliers and correspond to $\pm 2.7\sigma$. The maximum point of deepening is denoted by the filled circle and confines the outliers. The horizontal dashed lines represent the time-averaged values of the maximum deepening (red), the median deepening (dark blue), and the erosion area (light blue). Please note that the scaling of the vertical axis is not consistent between the plots and changes with the magnitude of the erosion. The time-averaged statistical quantities of the measured deepening are presented in Table 4.

On average, the diversity of the deepening was in the order of one magnitude for all experiments. Moreover, the measurements indicate that the deepening followed a consistent pattern in four out of six measurements, with the largest impact happening in the first third, followed by a general decrease over time (Figure 12). Only the second presented shear stress of EII (Figure 12d) and EIII (Figure 12f) oppose this trend and show large impacts in the second and last third, respectively. Generally, large impacts are often confined to just a few time steps during temporal progression, but then clearly exceed the time-averaged values (Figure 12). In EI the time-averaged median was exceeded by the maximum measured deepening by a factor of 13.3 during τ = 0.17 Pa (at 30 s), whereas during τ = 0.22 Pa it was exceeded by a factor of 16.0 (at 90 s). In EII the equally evaluated factors result in 7.0 (at 60 s) and 10.5 (at 60 s) during τ = 0.38 and 0.50 Pa, respectively. Finally, the time-averaged median of EIII was exceeded by the maximum measured deepening by a factor of 9.8 during a shear stress of τ = 0.65 Pa (at 150 s), whereas it was exceeded by a factor of 12.3 during τ = 0.81 Pa (at 540 s).

Overall, the results show that the distribution of the deepening had a consistently positive skew, since the upper whiskers in each of the boxplots are longer and the time-averaged mean is constantly higher than the median (Figure 12). This is further represented by the time-averaged maximum erosion compared to the median and underlines that the erosion was not normally distributed (Table 4).

The boxplots are plotted alongside the percentage of aggregated erosion area, which is the area within the ROI that experiences erosion. Table 5 presents the time-averaged and the maximum detected erosion areas. The results indicate that the time-averaged mean area affected by erosion is small with regard to the total area of the ROI (Table 5). Out of all six results, it was never exceeded by more than eight events (Figure 12b). Finally, a large erosion area does not necessarily coincide with a large deepening. While large area and deepening coincide in EII and EIII, this is not the case for EI and thus suggests an influence of the erosion behaviour.

Temporal development of erosion rates for selected time periods

Figures 13a–f show the temporal development of the erosion rates (ε) for the time periods, with a characteristic temporal change in the erosion behaviour for EI, EII, and EIII (see also Table 3 and Figure 12). They are all related to the entire area of the chosen ROI (A_{ROI} = 2642 mm^2). Furthermore, the erosion rates are presented for the following five time intervals: dt = 15, 30, 60, 100, and 120 s (denoted by different colours), to encompass those time intervals used in the previous evaluations. The erosion rates are shown on a semi-logarithmic plot to account for the large range of variations. Further, the erosion rates contain blank time steps in the event that no erosion rate was detected. The horizontal dashed line in each graph denotes the time-averaged erosion rates obtained with dt = 100 s. Table 6 summarises these time-averaged mean erosion rates and the maximum detected erosion rate next to their time period of occurrence.

It is shown in Figure 13 that small time intervals reveal a fluctuating trend and indicate that the erosion rates can vary significantly during temporal progression (e.g. Figures 13a, b, and d). On the contrary, large time intervals provide an averaged erosion rate due to integration over a longer period and are thus capable of measuring low rates (e.g. Figures 13e and f). Figure 13c presents only an initial response followed by two individual measured erosion rates as a result of hardly existing erosion, and confirms previous knowledge (e.g. Figure 5g).

On average, the diversity of the detected erosion rates is one order of magnitude in Figures 13a and c, whereas it is two orders of magnitude in Figures 13b, d, e, and f. High erosion rates were predominantly detected in the first third (Figures 13a, b, c, and e), but also notably in the second third (Figure 13d) and in the final third (Figure 13f) of the measurement (see also Table 6). By using existing erosion types, the rates presented in Figure 13c can be classified as erosion *Type I* (depth-dependent). The rates in Figures 13a, b, and e share features of *Type I* and *Type II* erosion, with the highest rates being detected at the beginning, but ultimately the erosion did not cease. The erosion rates presented in Figures 13d and f do not follow *Type I* (depth-limited) or *Type II* (steady-state) erosion within the considered period of time, and thus cannot be classified with the common erosion types.

Discussion of Results

The high spatio-temporal resolution measurements provide the means to distinguish between two fundamental erosion processes caused by specific erosion forms, which could be measured and identified in our experiments: (i) the emergence of individual erosion spots as a result of surface erosion (i.e. floc and aggregate entrainment) and (ii) the formation of large holes torn open by detached aggregate chunks (Figures 6 and 7). Whereas individual erosion spots were a recurring phenomenon that could be continuously measured during low and high shear stresses, large erosion holes were measured primarily at shear stresses that exceeded τ = 0.38 Pa (Figure 5). The chronology of these processes and their causing specific erosion forms are in qualitative agreement with the observations of many authors (e.g. Parchure and Mehta, 1985; Amos *et al.*, 1992; Mitchener and Torfs, 1995; McNeil *et al.*, 1996; Roberts *et al.*, 2003; Debnath *et al.*, 2007; Righetti and Lucarelli, 2007; Jacobs *et al.*, 2011). Given the photogrammetric approach and the available time series of frames, the specific erosion forms can always be verified by overviewing the raw data (e.g. Figure 4).

The temporal development of the erosion experiments reveals interrelated processes, namely (iii) the propagation of the erosion in the longitudinal and lateral direction, leading eventually to a merging of disconnected erosion areas, and (iv) progressive vertical erosion of already affected areas (Figures 8–10). Understandably, processes (iii) and (iv) are a

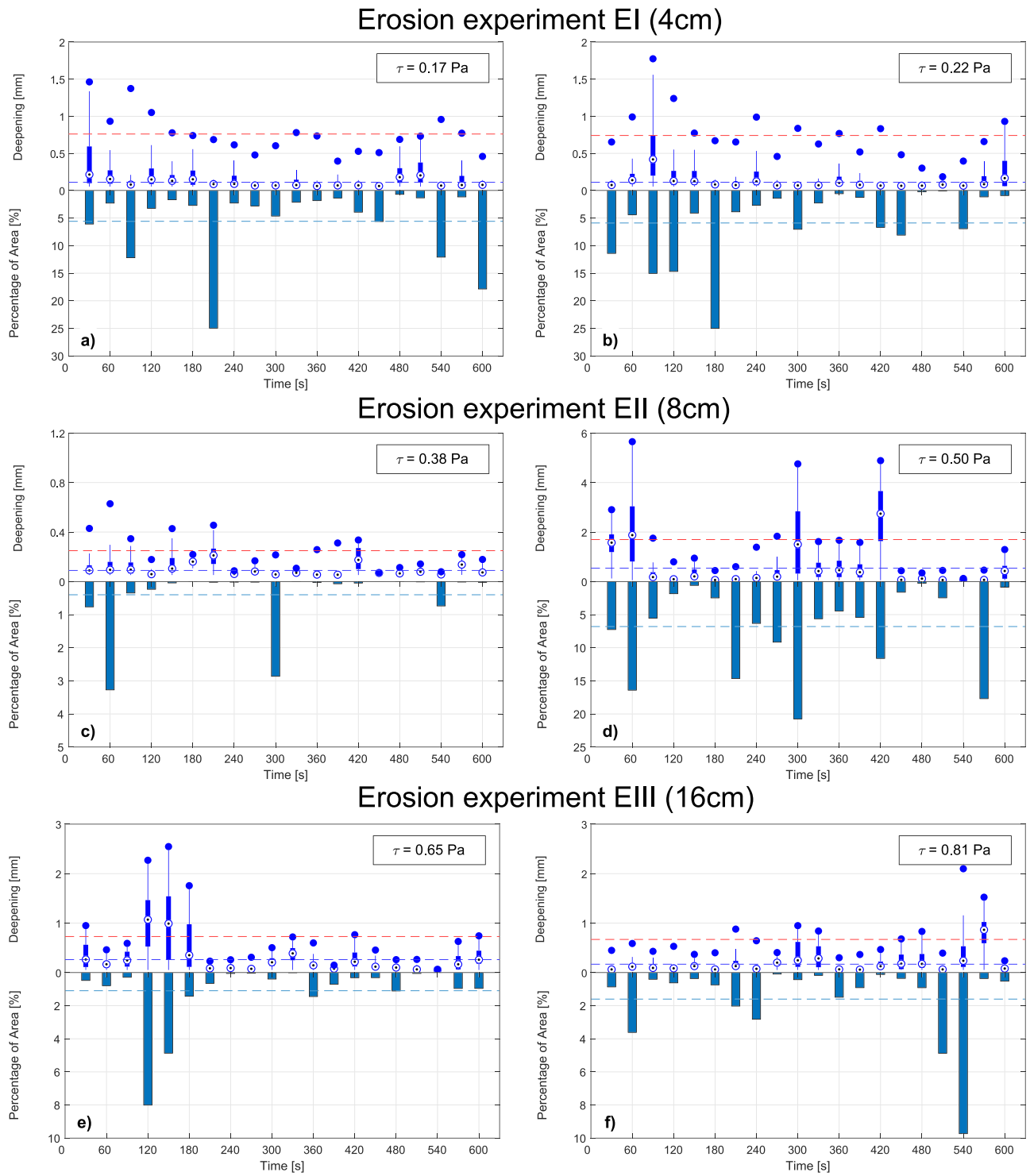

Figure 12. Spatio-temporal variability of the measured deepening per pixel plotted over the percentage of affected erosion area with respect to the entire ROI (A_{ROI} = 2642 mm^2; 580800 pixels). Results are shown for two consecutive shear stresses per experiment EI (4 cm), EII (8 cm), and EIII (16 cm). The horizontal dashed lines denote the time-averaged maximum deepening (red), the median deepening (dark blue), and the erosion area (light blue). [Colour figure can be viewed at wileyonlinelibrary.com]

logical temporal consequence during ongoing erosion, but in contrast to non-cohesive sediments, these processes have been insufficiently studied on relevant scales due to the fact that high spatio-temporal resolution data of cohesive sediment erosion were very limited or completely unavailable (e.g. Tolhurst *et al.*, 2006). However, these processes should be addressed, since erosion is a self-reinforcing process and likely progresses from already affected erosion areas as confirmed throughout Figures 5–10.

As a result of the high-resolution data obtained, the profile of the erosion volume can be complemented with the profiles of the affected erosion area, the specific deepening, and the number of disconnected erosion areas to take into consideration spatial information (Figure 11). While the specific deepening is a quantitative parameter that provides information on the significance of an occurring erosion, the number of disconnected erosion areas is a solely qualitative parameter as it contains no information on the actual erosion magnitude. Still, it is a robust variable that intuitively provides information on the spatial distribution of the erosion within a considered area (in this study, the ROI). Further, the incipient rise of the disconnected erosion areas marks the initiation of surface erosion (Figure 11d), as the

Table 4. Time-averaged statistical quantities of deepening for the selected shear stresses per erosion experiment. The median is denoted by $\widetilde{\Delta z^{(j)}}$, the mean by $\overline{\Delta z^{(j)}}$, the standard deviation by SD, and the maximum values by $\overline{\Delta z_{max}^{(j)}}$

Name	Sediment layer (cm)	Shear stress (Pa)	$\widetilde{\Delta z^{(j)}}$ (mm)	$\overline{\Delta z^{(j)}}$ (mm)	SD (mm)	$\overline{\Delta z_{max}^{(j)}}$ (mm)
		0.17	0.11	0.15	0.12	0.76
EI	4	0.22	0.11	0.15	0.11	0.74
		0.38	0.09	0.10	0.04	0.25
EII	8	0.50	0.54	0.58	0.39	1.70
		0.65	0.26	0.28	0.17	0.73
EIII	16	0.81	0.17	0.20	0.12	0.67

Table 5. Time-averaged erosion area $\left(\overline{A_e}\right)$ and maximum detected erosion area ($A_{e,max}$) with respect to the entire area of the ROI (A_{ROI} = 2642 mm^2) for the selected shear stresses per erosion experiment

Name	Sediment layer (cm)	Shear stress (Pa)	$\overline{A_e}$ (%)	$A_{e,max}$ (%)
		0.17	5.6	25.0
EI	4	0.22	5.9	25.0
		0.38	0.4	3.3
EII	8	0.50	6.8	20.8
		0.65	1.1	8.0
EIII	10	0.81	1.6	9.7

variable counts already the emerging individual erosion spots (process (i)). It is worth noting that surface erosion (flocs, small aggregates) marginally contributes to the total erosion volume (Figure 11a). Conversely, initiation of surface erosion could not readily be deduced from the time series of the erosion volume. A drop in the disconnected erosion areas, combined with an increasing erosion volume and erosion area, is evidence of a change in the erosion behaviour and implies that processes (iii) and (iv) are present.

A characteristic increase in the specific deepening indicates erosion events of high significance. Such an increase is most distinct in EII and EIII, since deep holes were torn open by the sudden detachment of aggregate chunks (process (ii); see also Figures 5e–l). Similar effects have been visually observed (but not dynamically measured) by various authors. For example, Mitchener and Torfs (1995) reported aggregated clumps of material being removed from a cohesive surface, McNeil *et al*. (1996) reported chunks of eroded sediment that leave holes or pits behind, and Zhu *et al*. (2008) referred to clusters and lumps of aggregates during erosion (see also Debnath *et al*., 2007; Aberle, 2008). Although no uniform terms are used, the specific erosion forms described are likely to be the same. Certainly, such events will result in the same erosion process, namely the formation of large holes, which is reflected in the specific deepening of EII and EIII (Figure 11; see also Figures 5e–l).

The necessity to address the spatial distribution alongside the eroded volume is reflected by cross-comparing the results of EI, EII, and EIII (Figure 11). When taking into account the erosion volume only (Figure 11a), misinterpretations of erosion data can be a consequence as the development suggests a resemblance among erosion experiments EI and EII. In general, erosion volume profiles can only be evaluated with regard to an initial rise, a change in the slope, and the final eroded (bulk) volume. Thus, it is not possible to assess the spatial distribution of the occurring erosion nor to obtain information on the dominant erosion process, making user-specific descriptions necessary (e.g. Mehta and Partheniades, 1982; Amos *et al*., 1992; Mitchener and Torfs, 1995; Debnath *et al*., 2007; Righetti and Lucarelli, 2007). Only with the addition of the affected erosion area (Figure 11b) and the specific deepening (Figure 11c) does it become obvious that the experiments EI and EII must have experienced erosion of different spatial extent and different behaviour.

As a whole, it is possible to draw conclusions on the erosion behaviour by means of erosion profiles, in case they contain spatial information. This is an integral finding of this study, since we obtained quantitative results which can be interpreted in terms of the dominant erosion forms and their spatial distribution without requiring supporting qualitative information (such as visual observations).

Based on the full temporal development of the erosion profiles per experiment (Figure 11), two consecutive shear stresses indicating a change in the erosion behaviour were (exemplarily) selected for detailed evaluations (see Figure 12, Tables 4 and 5). In general, the spatio-temporal erosion variability indicates that the distribution of the erosion is right-skewed and not normally distributed for all considered time steps and over all experiments (Figure 12 and Table 4). This corresponds to the general understanding of cohesive sediment erosion, since locally increased erosion is likely due to the mutual interference of surface changes and flow changes initiating progressing erosion (as confirmed by the detected processes (iii) and (iv) shown in Figures 8–10) (see also Van Prooijen and Winterwerp, 2010; Schäfer Rodrigues Silva *et al*., 2018). More specifically, the (now quantifiable) variability indicates that the deepening can vary significantly during temporal progression. When relating the maximum measured deepening to the time-averaged median, this results in variability factors ranging from 7.0 to 16.0 (Figure 12). Such factors are reasonable, as it has been shown that strong impacts are mostly confined to a few erosion events. This is most evident for experiment EII during exposure to a shear stress of τ = 0.50 Pa, where three characteristic impacts at 60, 300, and 420 s dominate the erosion (Figure 12d). Each impact corresponds to one of the three large holes that were torn into the surface (cf. Figure 5h). As expected, the median and maximum detected deepening of each impact exceeded the time-averaged values considerably (Figure 12d, Table 4). These results make clear the significant variability of cohesive sediment erosion during temporal progression.

Another insight is that the largest deepening does not necessarily correlate with the largest measured erosion area. This can also be explained with the erosion behaviour and the dominant erosion processes. Individual emerging erosion spots induced by surface erosion may affect a large erosion area but usually do not result in a large deepening (e.g. Figure 12b). On the contrary, it is likely that large holes torn open by the sudden detachment of aggregate chunks (i.e. a large deepening) coincide with a large erosion area at this time step (e.g. Figure 12d). This emphasises the need to measure cohesive

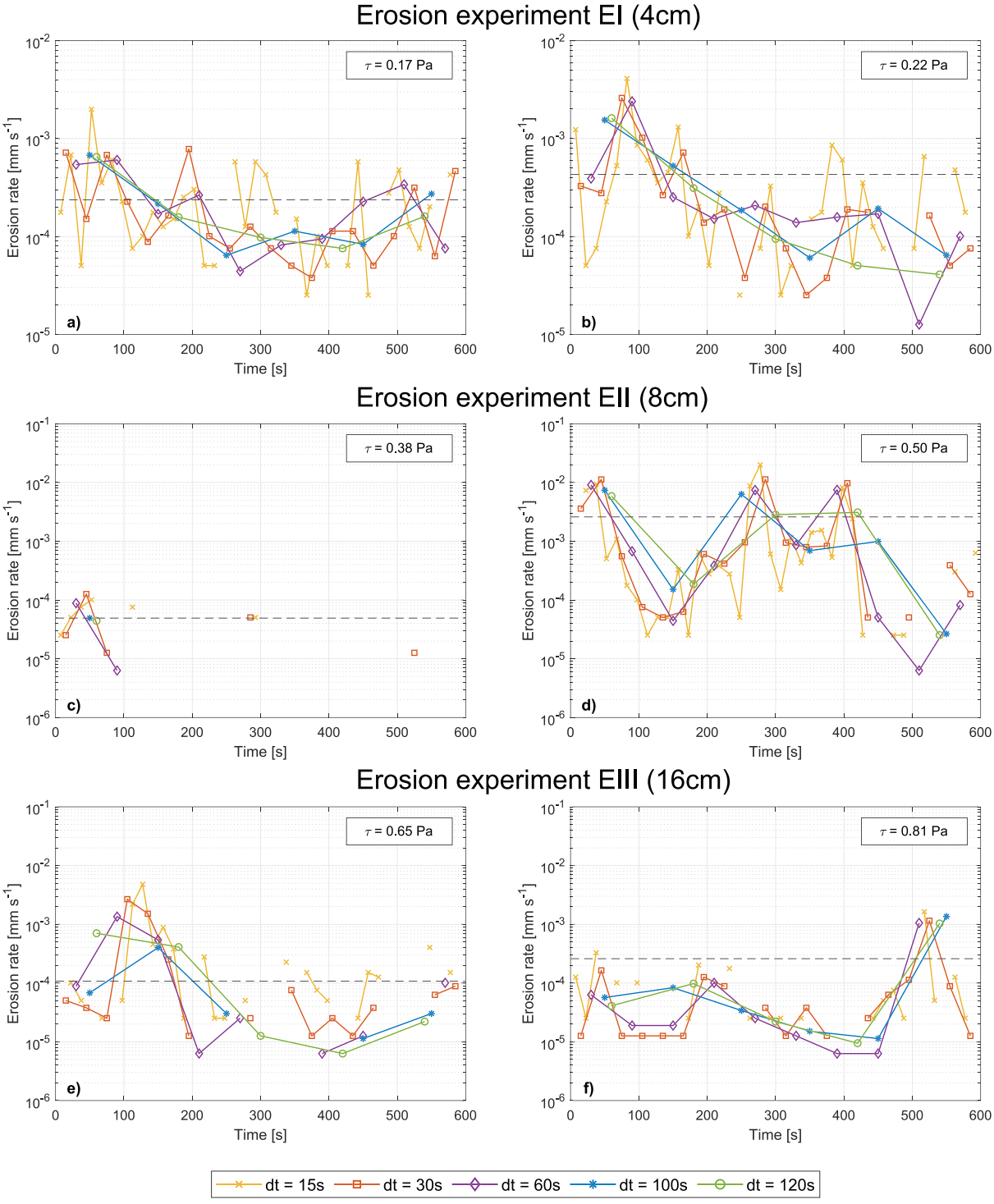

Figure 13. Erosion rates evaluated with respect to the entire ROI (A_{ROI} = 2642 mm^2) for five different time intervals (dt = 15, 30, 60, 100, 120 s). Results are shown for two consecutive shear stresses per experiment: EI (4 cm), EII (8 cm), and EIII (16 cm). The horizontal dashed line denotes the time-averaged erosion rate for dt = 100 s. [Colour figure can be viewed at wileyonlinelibrary.com]

sediment erosion, spatially resolved and with high resolution, to verify such relationships and the erosion processes responsible.

The need for high-resolution measurements is further reflected in the presented erosion rates (Figure 13). Four out of six presented erosion rates can be classified using common erosion types (*Type I* and *Type II*). The remaining two erosion rates presented in Figures 13d and f do not follow one of these existing types. This can be explained when comparing Figure 13 with the previous Figures 5–10. All peaks in the erosion rates, including the maximum rate detected, can be attributed to erosion events induced by specific processes. Among these are the emergence of individual erosion spots (e.g. Figures 13a and b; see also Figures 5c and d), as well as the formation of large holes, which were torn open by detached aggregate chunks (e.g. Figures 13d–f; see also Figures 5h–l). Since the common erosion types refer to resuspension rates (Mehta and Partheniades, 1982), an inability exists to classify aggregate chunks due to their highly probable bed load transport mode after detachment (e.g. Mitchener and Torfs, 1995; Roberts *et al.*, 2003; Debnath *et*

Table 6. Time-averaged mean erosion rates ($\bar{\varepsilon}$) obtained with dt = 100 s and maximum measured erosion rates (ε_{max}) as well as their time period of occurrence for the selected shear stresses per erosion experiment

Name	Sediment layer (cm)	Shear stress (Pa)	$\bar{\varepsilon}$ (mm s^{-1})	ε_{max} (mm s^{-1})	Time period (s)
		0.18	0.0002	0.002	45–60
EI	4	0.22	0.0004	0.041	75–90
		0.38	0.00005	0.0001	30–60
EII	8	0.51	0.0026	0.02	270–285
		0.65	0.0001	0.0048	120–135
EIII	10	0.80	0.0003	0.0016	510–525

al., 2007). As shown, such events occur within our data (particularly reflected in Figures 13d and f) as our measurements are insensitive to the transport mode after erosion (photogrammetric approach; erosion rates calculated using Equation 8). However, any information on the erosion processes cannot be deduced from erosion rate profiles. This underlines once again that there is a need for spatially resolved measurements. Only by considering additional spatial information is it possible to draw conclusions on the erosion behaviour and on the fundamental processes of cohesive sediment erosion.

A general assessment of the erosion experiments EI, EII, and EIII reveals that the erosion in EI is characterised by mainly (i) individual emerging erosion spots as a result of surface erosion and the further interrelated processes (iii) and (iv) (Figures 5a–d and 11–13). These observations suggest that the sediment sample has a vertical gradient in bed shear strength, leading to depth-limited or supply-limited erosion (e.g. Aberle, 2008) (i.e. *Type I* erosion), as proven in Figures 13a and b. This erosion type, in turn, is typical for stratified surficial sediment beds (Mehta and Partheniades, 1982), which are weakly consolidated. Due to the shallow sediment depth (4 cm) and sediment characteristics (Table 2), this holds true for EI. Consequently, our results confirm previous knowledge that surface erosion and further interrelated processes (such as (iii) and (iv)) are dominant in surficial and weakly consolidated sediment beds. The erosion of EII and EIII was mainly characterised by the formation of deep holes, which were torn into the surface through the detachment of aggregate chunks (Figures 5e–l and 11–13). Given the sediment depths (8 and 16 cm) and sediment characteristics (Table 2), we attribute this behaviour to a more consolidated bed. Although little information is available on the erosion behaviour of consolidated or compacted cohesive sediments (Zhu *et al*., 2008), this conclusion corresponds well to the visual observations of Debnath *et al*. (2007) and Aberle (2008), who report on large aggregates and lumps of material eroded from consolidated, cohesive beds. Furthermore, the remaining holes in the surface of EII and EIII (Figures 5h and l) resemble observations made with compacted sediment mixtures (e.g. pothole erosion described by Kothyari and Jain, 2008).

Overall, it can be concluded that the erosion decreased over depth (Figures 5 and 11) and thus with a higher bulk density, a refinement of the sediment composition, and a decreasing organic content (Table 2). This is in general agreement with previous knowledge on the erosion stability of natural non-cohesive/cohesive sediment mixtures (McNeil *et al*., 1996; Lick and McNeil, 2001; Righetti and Lucarelli, 2007; Schäfer Rodrigues Silva *et al*., 2018).

The potential limitations of this study were more commonly due to the erosion flume (SETEG) than to the applied photogrammetric method (PHOTOSED). One complication is the roughness transition from the smooth flume bed to the sediment surface. To counteract this issue, we selected our ROI with a minimum distance of 1.5 cm from the sediment core boundary (Figures 3 and 4), despite Roberts *et al*. (2003) concluding for a similar flume that the effect would be negligible and contribute minimally to overall experimental results. Further, the hydraulic calibration shown in Table 1 presents double-averaged shear stress values and their spatial standard deviations, which are 11% on average. Although a spatial distribution over the sample exists, this cannot explain the large measured erosion variability. The shear stress might also underestimate the effective near-bed Reynolds shear stress since the roughness of the sediment bed deviates during an erosion experiment (e.g. Berlamont *et al*., 1993; Black and Paterson, 1997; Aberle *et al*., 2006; Debnath *et al*., 2007; Aberle, 2008). Taking into account the effect of dynamic roughness changes induced by ongoing erosion, as well as turbulence-induced shear stress fluctuations, remains a topic for future research. To address these issues, high spatio-temporal resolution measurements are a crucial requirement, as geometric roughness changes of a surface can be derived from the dynamically measured erosion data (e.g. with the approach of Aberle *et al*., 2010). This enables us to study flow–sediment interactions and also to correlate turbulence intensities with erosion distribution functions.

Summary and Conclusions

The presented study demonstrates that due to the high spatio-temporal resolution of our method (PHOTOSED), it is possible to measure the erosion process of cohesive sediments and non-cohesive/cohesive sediment mixtures, dynamically and pixel-based with a vertical resolution in the sub-millimetre range. Consequently, we are able to detect and distinguish between two fundamental erosion processes: (i) the emergence of individual erosion spots caused by surface erosion and (ii) the formation of large holes that were torn open by detached aggregate chunks. Furthermore, interrelated processes as a temporal consequence of ongoing erosion were detected: (iii) the propagation of the erosion in the longitudinal and lateral direction, which eventually led to the merging of disconnected erosion areas and (iv) the progression of the erosion in the vertical direction (ongoing deepening).

It has further been shown that the ability to consider spatial information (such as erosion area, specific deepening, and number of disconnected erosion areas) – besides volumetric erosion profiles – allows us to draw conclusions on the erosion behaviour by quantitative means without requiring additional qualitative information. This is an essential requirement for a robust assessment of erosion data, which volumetrically resemble each other but ultimately experience a different erosion behaviour.

The evaluation of the spatio-temporal erosion variability for selected time periods revealed that the largest erosion events are confined to only a few time steps during temporal progression. In this event they exceeded the time-averaged median of the deepening significantly (factors between 7.0 and 16.0). It has been proven that the largest deepening does not necessarily coincide with the largest erosion area, since these relationships are controlled by the fundamental erosion processes and the specific erosion forms. On the contrary, such substantial information cannot be deduced from common (bulk) erosion rates. In summary, the findings emphasise the need for temporally and spatially resolved measurements – especially when addressing research topics in cohesive erosion research, such as the investigation of flow–sediment interactions.

In addition, for the three presented erosion experiments it can be concluded that (i) individual erosion spots caused by surface erosion and the interrelated processes (iii) and (iv) were

characteristic for the weakly consolidated sediment layer (4 cm), while (ii) the formation of large holes caused by detached aggregate chunks was characteristic for the more consolidated sediment layers (8 and 16 cm). Overall, the erosion decreased over sediment core depth and, thus, with a higher bulk density, a refinement of the sediment composition, and a decrease in organic content.

The key conclusion is that we measured fundamental erosion processes caused by specific emerging erosion forms, derived descriptive variables to consider spatial information in (bulk) erosion profiles, and quantified the spatio-temporal erosion variability (while minimising possible boundary effects by means of the photogrammetric approach). As a whole, this provides reliable high-resolution data of cohesive sediment erosion and the means for robust assessments of the erosion behaviour.

According to Grabowski *et al*. (2011) and Wu (2016), it is an essential prerequisite to generate comparable and more reliable (cohesive) erosion data from the field and laboratory. We add that this data should be of high spatio-temporal resolution. Therefore, we recommend developing and implementing the use of more high spatio-temporal resolution measurements in cohesive sediment research. This will serve towards a common goal: to give rise to further dependable erosion data that will develop deeper insights into the complex erosion of cohesive sediments and non-cohesive/cohesive sediment mixtures.

Acknowledgements—This study was carried out within the project CHARM – Challenges of Reservoir Management – Meeting Environmental and Social Requirements. The project is part of the Water Research Network Baden-Württemberg. It is funded by the Ministry of Science, Research, and Arts of the federal state of Baden-Württemberg, Germany.

We gratefully acknowledge the help of Ruslan Biserov, who conducted various time-consuming erosion experiments. We would also like to thank Kaan Koca, Sergey Oladyshkin, and James Nodwell-Taylor for their valuable assistance.

Conflict of Interest

The authors have no conflict of interest to declare.

Data Availability STATEMENT

The data sets used and/or analysed during the current study are available from the corresponding author on reasonable request.

References

Aberle J. 2008. Measurement techniques for the estimation of cohesive sediment erosion, Hydraulic Methods for Catastrophes: Floods, Droughts, Environmental Disasters. Publications of the Institute of Geophysics, Polish Academy of Sciences.

AberleJ., Nikora V., Henning M., Ettmer B., Hentschel B.. 2010. Statistical characterization of bed roughness due to bed forms: A field study in the Elbe River at Aken, Germany. *Water Resources Research*, **46**(3), W03521. https://doi.org/10.1029/2008wr007406.

Aberle J, Nikora V, Walters R. 2006. Data interpretation for in situ measurements of cohesive sediment erosion. *Journal of Hydraulic Engineering* **132**: 581–588. https://doi.org/10.1061/(ASCE)0733-9429(2006)132:6(581).

Aberle J, Nikora V, Walters R. 2004. Effects of bed material properties on cohesive sediment erosion. *Marine Geology* **207**: 83–93. https://doi.org/10.1016/j.margeo.2004.03.012.

Amos CL, Daborn GR, Christian HA, Atkinson A, Robertson A. 1992. In situ erosion measurements on fine-grained sediments from the Bay of Fundy. *Marine Geology* **108**: 175–196. https://doi.org/10.1016/0025-3227(92)90171-D.

Beckers F, Haun S, Noack M. 2018. Experimental investigation of reservoir sediments. *E3S Web Conferences* **40**: art. 03030. https://doi.org/10.1051/e3sconf/20184003030.

Berlamont J, Ockenden M, Toorman E, Winterwerp J. 1993. The characterisation of cohesive sediment properties. *Coastal Engineering* **21**: 105–128.

Black KS, Paterson DM. 1997. Measurement of the erosion potential of cohesive marine sediments: a review of current in situ technology. *Journal of Marine Environmental Engineering* **4**: 43–83.

Black KS, Tolhurst TJ, Paterson DM, Hagerthey SE. 2002. Working with natural cohesive sediments. *Journal of Hydraulic Engineering* **128**: 2–8.

Briaud JL, Ting FCK, Chen HC, Cao Y, Han SW, Kwak KW. 2001. Erosion function apparatus for scour rate predictions. *Journal of Geotechnical and Geoenviromental Engineering* **127**: 105–113. https://doi.org/10.1061/(ASCE)1090-0241(2001)127:2(105).

Debnath K, Nikora V, Aberle J, Westrich B, Muste M. 2007. Erosion of cohesive sediments: resuspension, bed load, and erosion patterns from field experiments. *Journal of Hydraulic Engineering* **133**(5) 508–520. https://doi.org/10.1061/(ASCE)0733-9429(2007)133:5(508).

DIN EN 13137. 2001. Characterization of waste – determination of total organic carbon (TOC) in waste, sludges and sediments. European Standard.

Droppo IG, D'Andrea L, Krishnappan BG, Jaskot C, Trapp B, Basuvaraj M, Liss SN. 2015. Fine-sediment dynamics: towards an improved understanding of sediment erosion and transport. *Journal of Soils and Sediments* **15**: 467–479. https://doi.org/10.1007/s11368-014-1004-3.

Farnebäck G. 2003. Two-frame motion estimation based on polynomial expansion. In *Image Analysis*, Bigun J, Gustavsson T (eds). Springer: Berlin; 363–370.

Gerbersdorf SU, Jancke T, Westrich B. 2007. Sediment properties for assessing the erosion risk of contaminated riverine sites. An approach to evaluate sediment properties and their covariance patterns over depth in relation to erosion resistance. First investigations in natural sediments (11 pp). *Journal of Soils and Sediments* **7**: 25–35. https://doi.org/10.1065/jss2006.11.190.

Grabowski RC, Droppo IG, Wharton G. 2011. Erodibility of cohesive sediment: the importance of sediment properties. *Earth Science Reviews* **105**: 101–120. https://doi.org/10.1016/j.earscirev.2011.01.008.

Gularte RC, Kelly WE, Nacci VA. 1980. Erosion of cohesive sediments as a rate process. *Ocean Engineering* **7**: 539–551. https://doi.org/10.1016/0029-8018(80)90051-7.

Hanson GJ, Cook KR. 2004. Apparatus, test procedures, and analytical methods to measure soil erodibility in situ. *Applied Engineering in Agriculture* **20** 455–462. https://doi.org/10.13031/2013.16492.

Jacobs W, Le Hir P, Van Kesteren W, Cann P. 2011. Erosion threshold of sand–mud mixtures. *Continental Shelf Research* **31**: S14–S25. https://doi.org/10.1016/j.csr.2010.05.012.

Kern U, Haag I, Schürlein V, Holzwarth M, Westrich B. 1999. Ein Strömungskanal zur Ermittlung der tiefenabhängigen Erosionsstabilität von Gewässersedimenten: das SETEG-System. *WasserWirtschaft* **89**: 72–77.

Kimiaghalam N, Clark SP, Ahmari H. 2016. An experimental study on the effects of physical, mechanical, and electrochemical properties of natural cohesive soils on critical shear stress and erosion rate. *International Journal of Sediment Research* **31**: 1–15. https://doi.org/10.1016/j.ijsrc.2015.01.001.

Kothyari UC, Jain RK. 2008. Influence of cohesion on the incipient motion condition of sediment mixtures. *Water Resources Research* **44**: W04410. https://doi.org/10.1029/2007WR006326.

Lick W, McNeil J. 2001. Effects of sediment bulk properties on erosion rates. *Science of the Total Environment* **266**: 41–48. https://doi.org/10.1016/S0048-9697(00)00747-6.

McNeil J, Taylor C, Lick W. 1996. Measurements of erosion of undisturbed bottom sediments with depth. *Journal of Hydraulic Engineering* **122**: 316–324. https://doi.org/10.1061/(ASCE)0733-9429(1996)122:6(316).

Mehta AJ, Partheniades E. 1982. Resuspension of deposited cohesive sediment beds. In *Proceedings of the 18th Conference on Coastal Engineering*, Cape Town; 1569–1588.

Mitchener H, Torfs H. 1995. Erosion of mud–sand mixtures. *Coastal Engineering* **29**: 1–25. https://doi.org/10.1016/S0378-3839(96)00002-6.

Mostafa TS, Imran J, Chaudhry MH, Kahn IB. 2008. Erosion resistance of cohesive soils. *Journal of Hydraulic Research* **46**: 777–787. https://doi.org/10.1080/00221686.2008.9521922.

Nikora V, McLean S, Coleman S, Pokrajac D, McEwan I, Campbell L, Aberle J, Clunie D, Koll K. 2007. Double-averaging concept for rough-bed open-channel and overland flows: applications. *Journal of Hydraulic Engineering* **133**: 884–895. https://doi.org/10.1061/(ASCE)0733-9429(2007)133:8(884).

Nikuradse J. 1932. Gesetzmäßigkeiten der turbulenten Strömung in glatten Rohren. Forschung auf d. Gebiete d. Ingenieurwesens 3, 1-36. In German (English version in NASA TT F–10, 359,1966).

Noack M, Gerbersdorf S, Hillebrand G, Wieprecht S. 2015. Combining field and laboratory measurements to determine the erosion risk of cohesive sediments best. *Water* **7**: 5061–5077. https://doi.org/10.3390/w7095061.

Noack M, Schmid G, Beckers F, Haun S, Wieprecht S. 2018. PHOTOSED—PHOTOgrammetric Sediment Erosion Detection. *Geosciences* **8**: 243. https://doi.org/10.3390/geosciences8070243.

Panagiotopoulos I, Voulgaris G, Collins MB. 1997. The influence of clay on the threshold of movement of fine sandy beds. *Coastal Engineering* **32**: 19–43. https://doi.org/10.1016/S0378-3839(97)00013-6.

Parchure TM, Mehta AJ. 1985. Erosion of soft cohesive sediment deposits. *Journal of Hydraulic Engineering* **111**: 1308–1326. https://doi.org/10.1061/(ASCE)0733-9429(1985)111:10(1308).

Paterson DM. 1989. Short-term changes in the erodibility of intertidal cohesive sediments related to the migratory behavior of epipelic diatoms. *Limnology and Oceanography* **34**: 223–234. https://doi.org/10.4319/lo.1989.34.1.0223.

Perera C, Wu W. 2016. Erosion coefficients of cohesive sediments. In *Proceedings of World Environmental and Water Resources Congress 2016*, West Palm Beach, FL; 293–302.

Raudkivi AJ, Tan SK. 1984. Erosion of cohesive soils. *Journal of Hydraulic Research* **22**: 217–233. https://doi.org/10.1080/00221688409499380.

Righetti M, Lucarelli C. 2007. May the Shields theory be extended to cohesive and adhesive benthic sediments? *Journal of Geophysical Research* **112**: C05039. https://doi.org/10.1029/2006JC003669.

Roberts JD, Jepsen RA, James SC. 2003. Measurements of sediment erosion and transport with the adjustable shear stress erosion and transport flume. *Journal of Hydraulic Engineering* **129**: 862–871. https://doi.org/10.1061/(ASCE)0733-9429(2003)129:11(862).

Schäfer Rodrigues Silva A, Noack M, Schlabing D, Wieprecht S. 2018. A data-driven fuzzy approach to simulate the critical shear stress of mixed cohesive/non-cohesive sediments. *Journal of Soils and Sediments* **18**: 3070–3081. https://doi.org/10.1007/s11368-017-1860-8.

Tolhurst TJ, Defew EC, de Brouwer JFC, Wolfstein K, Stal LJ, Paterson DM. 2006. Small-scale temporal and spatial variability in the erosion threshold and properties of cohesive intertidal sediments. *Continental Shelf Research* **26**: 351–362. https://doi.org/10.1016/j.csr.2005.11.007.

TSI Inc. 2011. *Phase Doppler Particle Analyzer (PDPA)/Laser Doppler Velocimeter (LDV) – Operations Manual*, P/N 1990048, Revision G. TSI, Inc.: Shoreview, MN.

Van Prooijen BC, Winterwerp JC. 2010. A stochastic formulation for erosion of cohesive sediments. *Journal of Geophysical Research* **115**: C01005. https://doi.org/10.1029/2008JC005189.

Walder JS. 2016. Dimensionless erosion laws for cohesive sediment. *Journal of Hydraulic Engineering* **142**: 04015047. https://doi.org/10.1061/(ASCE)HY.1943-7900.0001068.

Wentworth CK. 1922. A scale of grade and class terms for clastic sediments. *Journal of Geology* **30**: 377–392.

Witt O, Westrich B. 2003. Quantification of erosion rates for undisturbed contaminated cohesive sediment cores by image analysis. *Hydrobiologia* **494**: 271–276. https://doi.org/10.1023/A:1025495122246.

Wu W. 2016. Mixed cohesive and noncohesive sediment transport: a state of the art review. In *River Sedimentation: Proceedings of the 13th International Symposium on River Sedimentation*: 9–18. ISRS: Stuttgart.

Wu W, Perera C, Smith J, Sanchez A. 2018. Critical shear stress for erosion of sand and mud mixtures. *Journal of Hydraulic Research* **56**: 96–110. https://doi.org/10.1080/00221686.2017.1300195.

Ye Z, Cheng L, Zang Z. 2011. Experimental study of erosion threshold of reconstituted sediments. In *ASME 2011 30th International Conference on Ocean, Offshore and Arctic Engineering*. ASME: Rotterdam; 973–983.

Zhu Y, Lu J, Liao H, Wang J, Fan B, Yao S. 2008. Research on cohesive sediment erosion by flow: an overview. *Science in China, Series E: Technological Sciences* **51**: 2001–2012. . https://doi.org/10.1007/s11431-008-0232-4.

